frontiers in Materials

ORIGINAL RESEARCH
published: 15 September 2021
doi: 10.3389/fmats.2021.732931

Effect of Acidizing Process on the Stress Corrosion Cracking of HP-13Cr Stainless Steel in the Ultra-depth Well Environment

Wenlong Qi, Yang Zhao, Tao Zhang and Fuhui Wang*

Shenyang National Laboratory for Materials Science, Northeastern University, Shenyang, China

The effect of acidizing process on the stress corrosion cracking of HP-13Cr stainless steel in the ultra-depth well environment was studied by the slow strain rate test, the electrochemical measurement, the microstructure observation, and the finite element modeling. The results indicated that the acidizing process significantly increased the stress corrosion cracking susceptibility of HP-13Cr stainless steel and induced the fracture mode to the brittle characteristic in the high temperature and CO_2 pressure environment. The stress corrosion cracking susceptibility also increased with the increase of temperature and CO_2 pressure. There were dense defects including pits and cracks in the fracture section from the transverse view. After the acidizing process, under tensile stress condition, the increasing roughness will cause the stress concentration and promote the local anodic dissolution, which induces the initiation of stress corrosion cracking.

Keywords: key word: acidification, HP-13Cr stainless steel, stress corrosion cracking, roughness, anodic dissolution

OPEN ACCESS

Edited by:
Jianbo Sun,
China University of Petroleum, China

Reviewed by:
Zhongyu Cui,
Ocean University of China, China
Liang Wu,
Chongqing University, China

****Correspondence:***
Tao Zhang
zhangtao@mail.neu.edu.cn

Specialty section:
This article was submitted to Environmental Degradation of Materials, a section of the journal Frontiers in Materials

Received: *29 June 2021*
Accepted: *06 August 2021*
Published: *15 September 2021*

Citation:
Qi W, Zhao Y, Zhang T and Wang F (2021) Effect of Acidizing Process on the Stress Corrosion Cracking of HP-13Cr Stainless Steel in the Ultra-depth Well Environment. Front. Mater. 8:732931. doi: 10.3389/fmats.2021.732931

INTRODUCTION

For the abundant oil and gas reservoir, ultra-depth well exploitation was widely carried out in northwestern China. The well depth was more than 8,000 m with carbonatite rocks and sandstone structures, which brings challenges to effective exploitation (Cui et al., 2004; Lan et al., 2015; Singh et al., 2017; Zhao et al., 2019a). On account of this, many methods such as hydraulic fracturing, steam-assisted gravity drainage, and acidizing are employed to enhance the property value by fast delivery of oil and gas fluid in a cost-effective manner. Among the above effective methods, acidizing has been recognized as the most accessible means to exploit the carbonate and sandstone reservoirs around the northwest of China (Mu and Zhao, 2010; Zhao et al., 2019a). However, the injection of lived acid (LA) during the acidizing process will cause severe corrosion of tubing and further affect the corrosion behavior of tubing in the formation water (FW), which is ejected from the geothermal environment during the exploitation process. The corrosion protection techniques, such as coating, inhibitors, and developing novel materials, are not effective in such an aggressive environment (Cui et al., 2021; Liu et al., 2021; Song et al., 2021). HP-13Cr stainless steel (SS), containing lower C and higher Ni and Mo than traditional 13Cr SS, was widely used as tubing material in the oil and gas industry because of its appropriate mechanical properties, excellent corrosion resistance, and cost-effectiveness. However, severe corrosion failures occurred after LA immersion.

The corrosion behavior of HP-13Cr SS during the acidizing process and in the FW has been investigated in recent years (Moreira et al., 2004; Mu and Zhao, 2010; Marcus, 2011; Qi et al., 2021; Cui et al., 2021; Liu et al., 2021; Song et al., 2021). (Zhang et al., 2020) built the Pourbaix diagram for

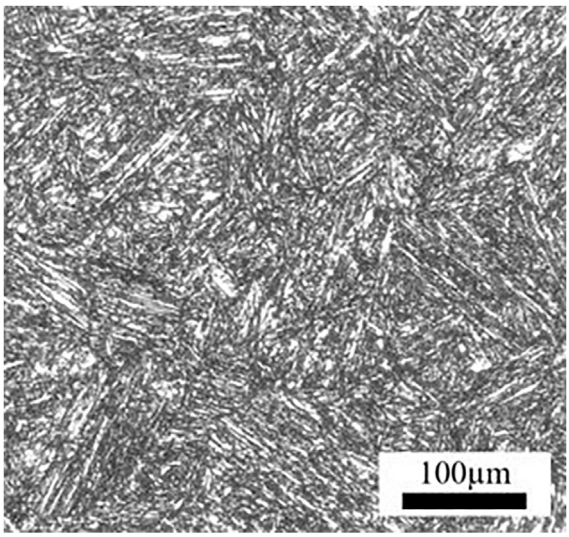

FIGURE 1 | The microstructure of HP-13Cr SS.

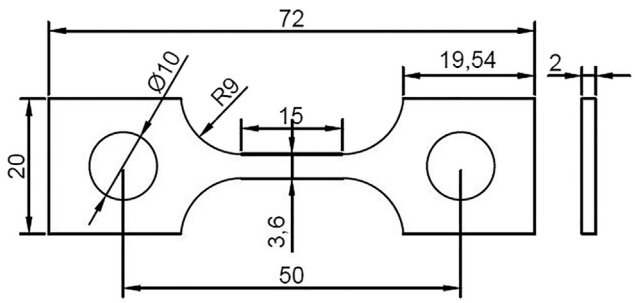

FIGURE 2 | Dimensions of the SSRT test specimen (unit, mm).

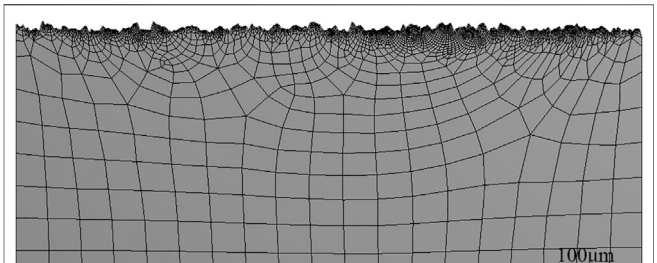

FIGURE 3 | Modeling and meshing of HP-13Cr SS surface after LA immersion.

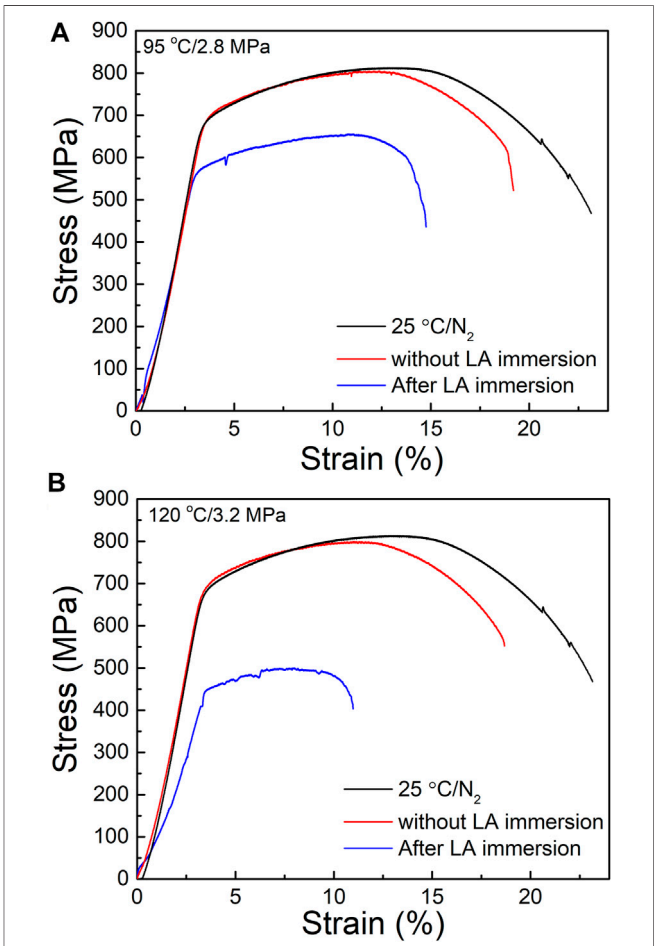

FIGURE 4 | Stress–strain curves of HP-13Cr SS in the FW at 25°C/N_2 atmosphere and at **(A)** 95°C/2.8MPa CO_2 and **(B)** 120°C/3.2 MPa CO_2 after LA immersion, respectively.

HP-13Cr SS in the aggressive FW and researched the general corrosion rate and pitting (Moreira et al., 2004; Marcus, 2011; Zhao et al., 2018; Li et al., 2019a; Li et al., 2019b; Zhao et al., 2019b; Qi et al., 2021; Cui et al., 2021; Liu et al., 2021). The effect of LA composition and the surface roughness on the corrosion behavior of HP-13Cr SS was also studied (Qi et al., 2021; Zhao et al., 2020). While many ultra-depth well tubes fractured due to stress corrosion cracking (SCC), further research interests should be shifted to SCC in the HTHP environment (Zhu et al., 2011; Lei et al., 2015; Zhang et al., 2019). The SCC susceptibility of HP-13Cr SS was up to 42% exposure at 150°C and 1 MPa CO_2 environment (Yue et al., 2018).

SCC of tubing materials in the high temperature, high CO_2 pressure, and high salinity environments evolved from localized corrosion such as pitting, which may induce the stress concentration (Isaacs, 1988; Cui et al., 2011; Zhao et al., 2012; Ramamurthy and Atrens, 2013; Wang and Han, 2013; Calabrese et al., 2015; Mai and Soghrati, 2017; Wang et al., 2019). Considering the effect of stress on the electrochemical reaction, Gutman built a mechano-electrochemical model to describe the effect of elastic and plastic deformation on the anodic dissolution of metals (Gutman, 1998). The applied stress can shift the pitting potential of 304 SS to a more negative value in 1 M HCl at room temperature (Suter et al., 2001). Meanwhile, the stress and strain concentration at the pitting area changed with the pitting morphology, determined by corrosive environments (Horner et al., 2011; Spencer et al., 2014; Parkins, 1996; Persaud et al., 2019; Lu et al., 2020). The LA

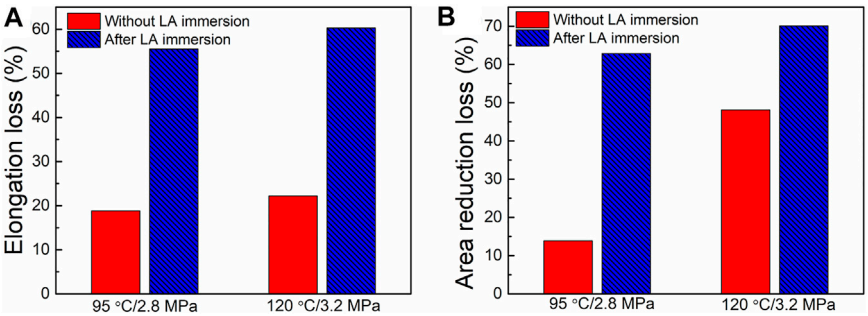

FIGURE 5 | SCC susceptibility of HP-13Cr SS. **(A)** elongation loss and **(B)** area reduction loss.

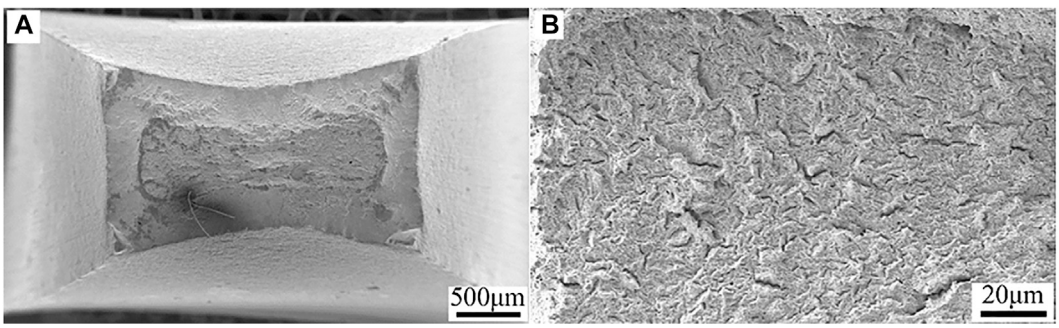

FIGURE 6 | Fracture morphologies of HP-13Cr SS viewed from the top after SSRT at 25°C/N_2 atmosphere. **(A)** low magnification and **(B)** high magnification.

immersion will result in many defects and larger roughness on the metal surface. It is not clear about the LA immersion on the SCC of HP-13Cr SS.

The aim of this work is to reveal the effect of the acidizing process, especially the LA process, on the SCC susceptibility of HP-13Cr SS in FW and clarify the interaction of surface roughness, water chemistry, and stress concentration on SCC by slow strain rate test (SSRT) (Henthorne, 2016), electrochemical measurements, micromorphology observation, and numerical simulation.

EXPERIMENTAL

Material and Solution

The material applied in this work is a commercial HP-13Cr SS, with a chemical composition (*wt*%) of Si 0.15, Mn 0.51, Cr 12.77, Mo 2.19, S 0.002, *p* 0.02, Cu 0.047, Ni 5.36, V 0.014, Al 0.037, and Fe balance. The yield strength is 700 MPa and the elongation is 21.6%. A typical tempered martensitic structure was observed in **Figure 1**. The dimension of the SSRT specimen was given in **Figure 2**. Prior to the experiment, the gauge section of the specimens was ground to 2000 grit abrasive paper along the tensile direction, then degreased with ethanol, washed with distilled water, and dried by the flow of air. The chemical composition of LA and FW have been listed in our previous work (Cui et al., 2021). Before the SSRT in FW, the specimen was immersed in LA for 6 h.

Slow Stain Rate Test

The slow stain rate test (SSRT) was carried out in the HTHP-SCC system at 95°C/2.8 MPa CO_2 and 120°C/3.2 MPa CO_2 FW conditions, with a strain rate of 10^{-6} s^{-1}. Before SSRT, the specimen was immersed in LA for 6 h at 95°C/2.8 MPa CO_2 and 120°C/3.2 MPa CO_2. There was also a SSRT as a normal group conducted at room temperature (25°C) and 0.1 MPa N_2 atmosphere.

The SCC susceptibility of the HP-13Cr SS was evaluated by the elongation loss ratio (I_δ) and reduction-in-area loss (I_ψ) according to the following **Eqs 1**, **2** (Tian et al., 2018):

$$I_\delta = \left(1 - \frac{\delta_s}{\delta_0}\right) \times 100\ \% \tag{1}$$

$$I_\psi = \left(1 - \frac{\psi_s}{\psi_0}\right) \times 100\ \% \tag{2}$$

where δ_s, ψ_s and δ_0, ψ_0 were the elongation and reduction-in-area of the HP-13Cr SS in the FW and at room temperature (25°C) and N_2 atmosphere, respectively.

Micromorphology Examination

The fracture surface of the HP-13Cr SS was cut off after removing the corrosion products based on ASTM standard G1-03 (ASTM, 2003). The fracture morphology viewed from the top and the transverse of the specimens was observed by SEM (Quanta 200 F, U.S.). The cross-section morphology of HP-13Cr SS after LA immersion has also been observed by SEM (Quanta 200 F, U.S.).

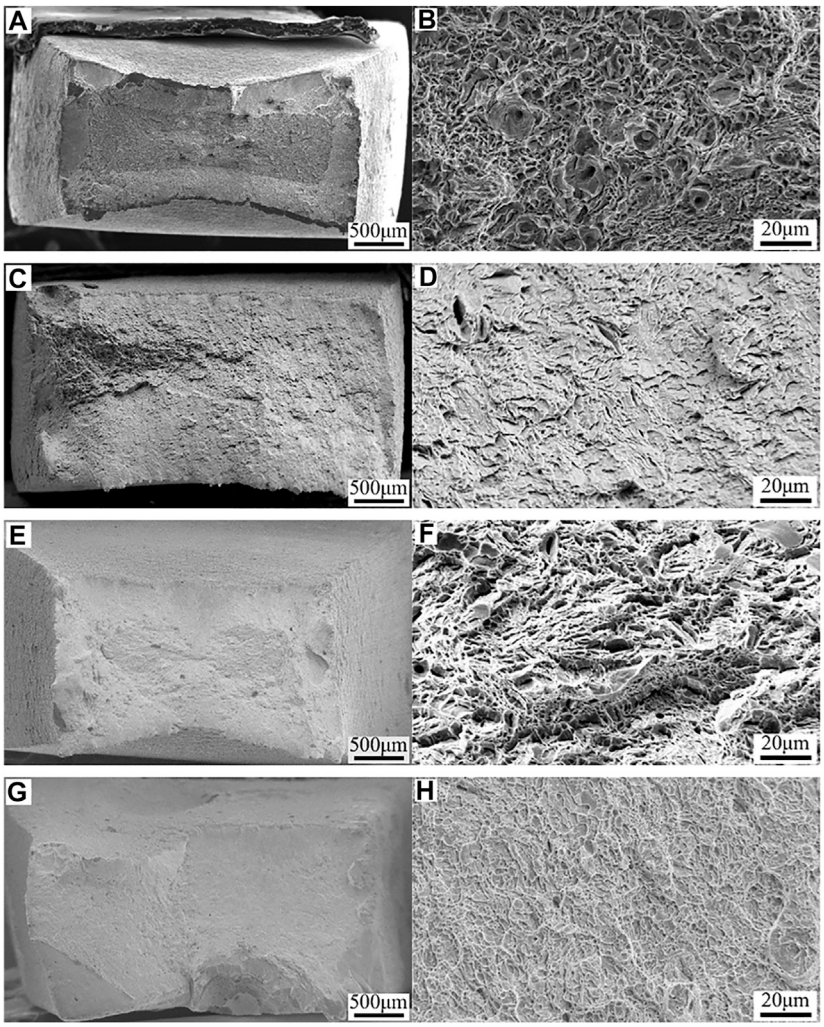

FIGURE 7 | Fracture morphologies of HP-13Cr SS viewed from the top after SSRT in FW at 95°C/2.8 MPa CO_2 without LA immersion at **(A)** low magnification and **(B)** high magnification, after LA immersion at **(C)** low magnification and **(D)** high magnification and 120°C/3.2 MPa CO_2 without LA immersion at **(E)** low magnification and **(F)** high magnification, after LA immersion **(G)** low magnification and **(H)** high magnification.

Electrochemical Measurement

The potentiodynamic polarization measurements were carried out in FW using the high temperature and high pressure static electrochemical measurement autoclave at 95°C/2.8 MPa CO_2 and 120°C/3.2 MPa CO_2, respectively (Li et al., 2019a). The specimen was also immersed in LA for 6 h before potentiodynamic polarization measurements.

The relationship between the electrode potential vs. standard hydrogen electrode (SHE) and the observed potential vs. the Ag/AgCl reference electrode is shown as **Eq. 3**,

$$E_{\mathrm{SHE}} = E_{\mathrm{obs}} + 0.2866 - 0.001\,(T - T_0) + 1.754 \times 10^{-7}\,(T - T_0)^2 - 3.03 \times 10^{-9}\,(T - T_0)^3 \tag{3}$$

where the E_{SHE} is the electrode potential vs. SHE, V; the E_{obs} is the observed potential vs. the Ag/AgCl reference electrode, V; T is the system temperature, K; and T_0 is the room temperature (25°C).

The potentiodynamic polarization curves swept from −0.3 V vs. open circuit potential (OCP) to 1.6 V vs. SHE with a scanning rate of 0.167 mV/s. To ensure reproducibility, identical experiments were repeated at least three times.

Numerical Simulation

The profile of HP-13Cr SS (OS) and HP-13Cr SS after immersion tests was observed by Ultra-Depth 3D Microscope (Olympus ILS4100, Japan). The roughness of surface was evaluated as S_a, which is the average absolute deviation of the roughness in a small area. S_a (μm) was defined as **Eq. 4**,

$$S_a = \left(\frac{1}{MN}\right)\sum_{i=1}^{M}\sum_{j=1}^{N}\left|Z_{ij}\right| \tag{4}$$

where M, N is the collected data points from two perpendicular directions in the measurement area; and Z_{ij} is the distance from the mean area to the number i j point.

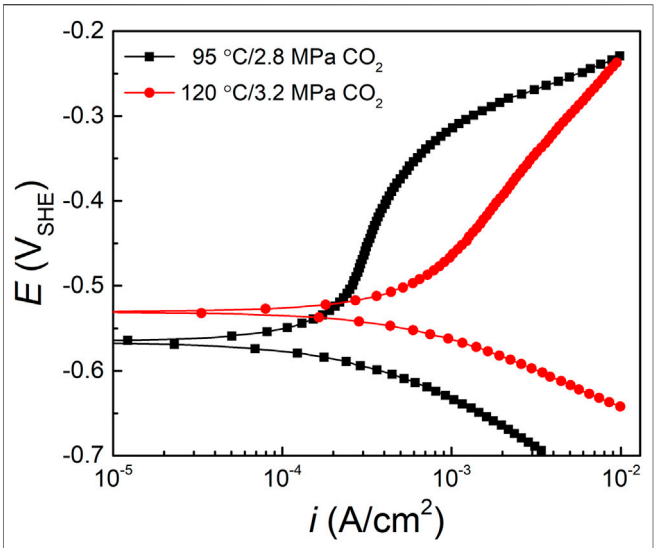

FIGURE 8 | Polarization curves of HP-13Cr SS after LA immersion in the FW at 95°C/2.8MPa CO_2 and 120°C/3.2 MPa CO_2.

TABLE 1 | Fitting electrochemical parameter of the potentiodynamic polarization curves of HP-13Cr SS after LA immersion in the FW at 95°C/2.8 MPa CO_2 and 120°C/3.2 MPa CO_2.

Temperature (°C)/CO_2 pressure (MPa)	E_{corr} (mV)	i_{corr} (×10^{-4} A/cm^2)
95/2.8	−564.61 ± 5.4	2.45 ± 0.25
120/3.2	−529.23 ± 6.6	4.14 ± 0.23

The tensile stress was set as 350 MPa (half of yield strength) by the finite element method (FEM) in **Figure 3**. The profile of the surface applied in the FEM was captured from the actual data of the specimen surface after LA immersion at 120°C/3.2 MPa. The mesh near the surface has been refined.

RESULT

SCC Susceptibility of HP-13Cr SS After LA Immersion

The stress-strain curves of HP-13Cr SS during SSRT were shown in **Figure 4**. Compared with the normal condition (25°C/N_2) and HP-13Cr SS without LA immersion, the curves of HP-13Cr SS drifted down dramatically and yielded at a low stress; meanwhile, the fracture occurred at a quite low strain. With the temperature and CO_2 pressure increasing from 95°C/2.8MPa to 120°C/3.2 MPa, the stress-strain curve further deteriorated.

The SCC susceptibility of HP-13Cr SS evaluated by I_δ and I_ψ was demonstrated in **Figure 5**. Compared to the mechanical property at normal conditions, with the temperature and CO_2 pressure increasing from 95°C/2.8 MPa to 120°C/3.2 MPa, I_δ and I_ψ increased from 18.8 to 22.2% and from 13.9 to 48.1% without LA immersion. While after an LA immersion, the I_δ increased to 55.5 and 60.3% and I_ψ increased to 62.9 and 70.1% at 95°C/2.8 MPa and 120°C/3.2 MPa, respectively. The dramatic increase of SCC susceptibility indicated that the LA process promoted the SCC of HP-13C SS in the FW environment and with the temperature and CO_2 pressure increasing, the mechanical properties are more severely reduced.

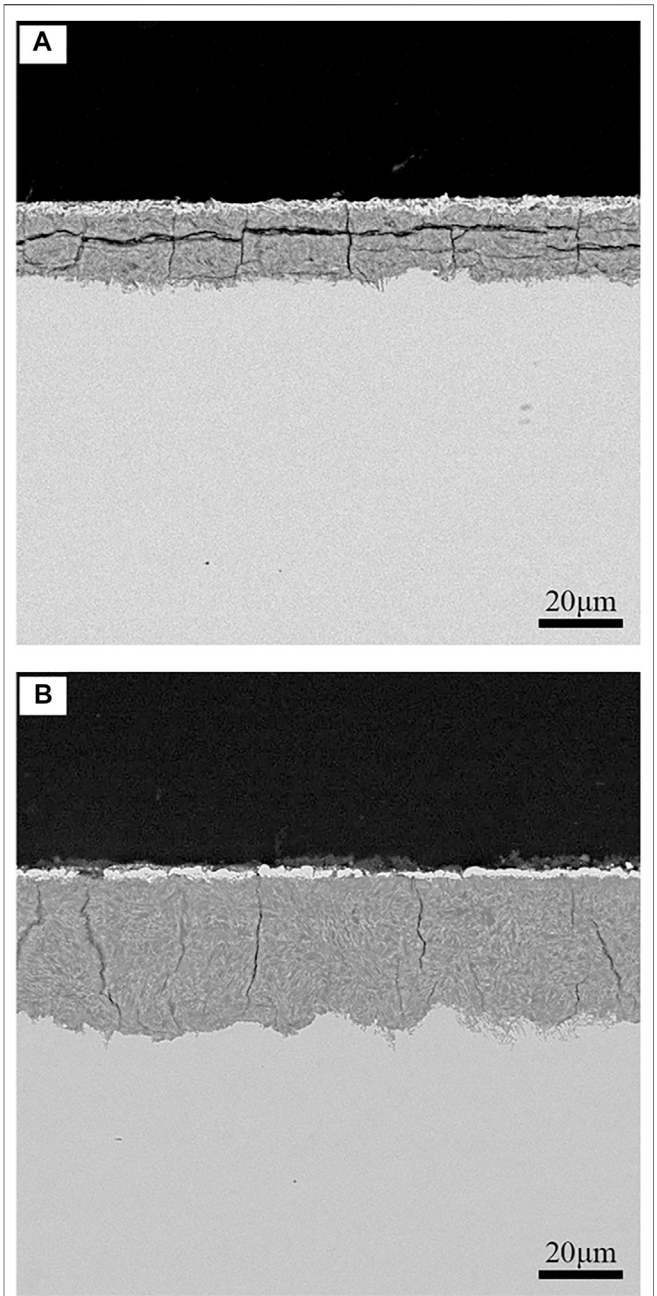

FIGURE 9 | Cross-sectional morphologies of HP-13Cr SS after LA immersion. **(A)** 95°C/2.8 MPa and **(B)** 120°C/3.2 MPa.

Fracture Morphology

The fracture morphologies of HP-13Cr SS viewed from the top after SSRT at normal conditions were illustrated in **Figure 6**. The

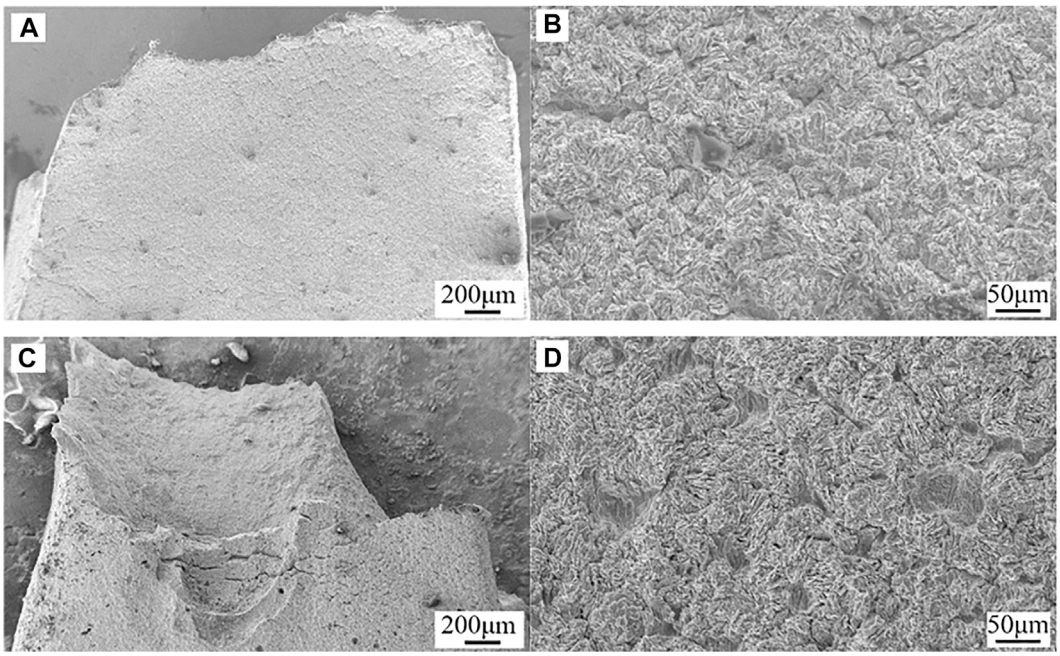

FIGURE 10 | Fracture morphologies of HP-13Cr SS after LA immersion and SSRT in the FW viewed from the transverse at 95°C/2.8MPa CO_2 **(A)** low magnification and **(B)** high magnification and 120°C/3.2 MPa CO_2 **(C)** low magnification and **(D)** high magnification.

TABLE 2 | Formula of the reaction equilibrium constants.

Equilibrium constants
$K_H = 14.46269 \times 10^{-(2.27+5.65\times10^{-3}T-8.06\times10^{-6}T^2+0.075I}$ (Duan and Li, 2008; Zhang and Cheng, 2009)
$K_{hyd} = 2.58 \times 10^{-3}$ (Duan and Li, 2008; Zhang and Cheng, 2009)
$K_{ca} = 387.6 \times 10^{-(6.41-1.594\times10^{-3}T+3.52\times10^{-6}T^2-3.07\times10^{-5}P-0.4772\sqrt{I}+0.1180I)}$ (Duan and Li, 2008; Zhang and Cheng, 2009)
$K_{bi} = 10^{-(10.61-4.97\times10^{-3}T+8.59\times10^{-6}T^2-7.00\times10^{-5}P-3.21\sqrt{I}+1.073I)}$ (Duan and Li, 2008; Zhang and Cheng, 2009)
$K_w = 10^{-(29.3868-0.0737549T+7.47881\times10^{-6}T^2)}$ (Duan and Li, 2008; Zhang and Cheng, 2009)

remarkable necking phenomena and typical cup-and-cone fracture, evidencing a high ductility, were observed (**Figure 6A**). There was a considerable amount of fine ductile dimples in corresponding high magnification figure (**Figure 6B**), indicating ductile fracture characteristics.

The fracture morphologies HP-13Cr SS without LA immersion showed a certain brittle fracture feature, including reduced necking at low magnification (**Figures 7A,E**) and reduced dimples and increased quasi-cleavage plane at high magnification (**Figures 7B,F**) at 95°C/2.8 MPa and 120°C/3.2 MPa FW. After LA immersion, most of the necking disappeared (**Figures 7C,G**) and the micromorphology showed a characteristic of brittle fracture with an almost flat plane (**Figures 7D,H**).

Electrochemical Behavior of HP-13Cr SS After LA Immersion in FW

The potentiodynamic polarization curves of HP-13Cr SS after LA immersion in the FW at 95°C/2.8 MPa CO_2 and 120°C/3.2 MPa CO_2 were shown in **Figure 8** and the fitting electrochemical parameters were listed in **Table 1** with the temperature and CO_2 pressure increasing from 95°C/2.8 MPa to 120°C/3.2 MPa, the corrosion potential (E_{corr}) slightly increased, and corrosion current (i_{corr}) doubled from 2.45 ± 0.25×10^{-4} A/cm^2 to 4.14 ± 0.23×10^{-4} A/cm^2. Since the corrosion production film formed after LA immersion, no significant passivation occurred, especially at 120°C/3.2 MPa FW.

DISCUSSION

The Initiation of SCC

The HP-13Cr SS in LA, as a quite low pH solution, will dissolve and fail to passivate (Zhao et al., 2019a). During LA immersion, the instant of the very thin and efficient corrosion-resistant passivating film as in the normal condition, a loose and thickness up to dozens of microns corrosion production film deposited on the surface, as the cross-sectional morphology after LA immersion shown in **Figure 9**. The corrosion production film

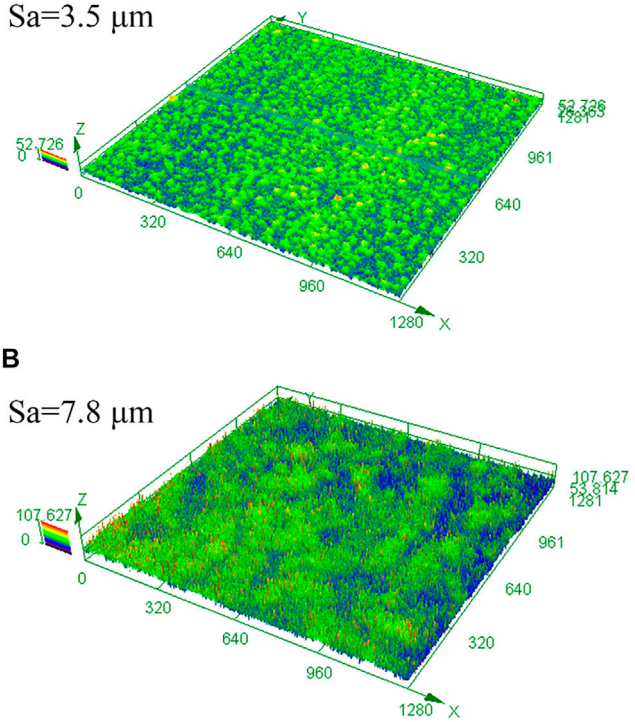

FIGURE 11 | 3D image and surface roughness of HP-13Cr SS after LA immersion. **(A)** 95°C/2.8 MPa and **(B)** 120°C/3.2 MPa.

was comprised of an outer layer rich in copper and comes from the inhibitors in LA solution and an $FeCO_3$ inner layer (Qi et al., 2021; Zhao et al., 2020). There were plenty of defects including cracking and partial holes. Under a tensile stress condition, the stress and strain will be concentrated in the defects to deteriorate the corrosion production film and the substrate metal under the film. Then, the pitting occurred as the origin of anodic dissolution cracking (Zhao et al., 2020).

The cracking and pitting can be observed from the fracture morphologies viewed from transverse in **Figure 10**. At 95°C/2.8 MPa CO_2, the cracking in the surface near the fracture area was dense and almost distributed perpendicular to the tensile direction. The cracking had a spindle shape and revealed a characteristic of anodic dissolution cracking. As the temperature and CO_2 pressure went up to 120°C/3.2 MPa, the cracking was longer and had a larger opening, indicating the greater anodic dissolution and more stress and strain concentration occurred after higher temperature and higher CO_2 pressure FA immersion.

The Interaction of Roughness, Water Chemistry, and Stress Concentration on the SCC

As a process of mechanical and electrochemical interaction, SCC was closely related to the water chemical environment. In the formation water, the equilibrium reactions during the CO_2 dissolution process and corresponding reaction equilibrium constants were listed as follows (Reaction **Eqs 5–9**) (Garsany et al., 2002; Nordsveen et al., 2003; Duan and Li, 2008; Zhang and Cheng, 2009),

$$CO_{2(g)} \rightleftharpoons CO_{2\ (aq)} \qquad K_H = \frac{C_{CO_{2(aq)}}}{\varphi P_{CO_{2(g)}}} \tag{5}$$

$$CO_{2(aq)} + H_2O_{(l)} \rightleftharpoons H_2CO_{3(aq)} \quad K_{hyd} = \frac{C_{H_2CO_{3(aq)}}}{C_{CO_{2(aq)}}} \tag{6}$$

$$H_2CO_{3(aq)} \rightleftharpoons H^+ + HCO_3^- \qquad K_{ca} = \frac{\gamma_{\pm 9}^2 C_{H^+} C_{HCO_3^-}}{C_{H_2CO_{3(aq)}}} \tag{7}$$

$$HCO_3^- \rightleftharpoons H^+ + CO_3^{2-} \qquad K_{bi} = \frac{\gamma_{\pm 10} C_{H^+} C_{CO_3^{2-}}}{C_{HCO_3^-}} \tag{8}$$

$$H_2O_{(l)} \rightleftharpoons H^+ + OH^- \qquad K_w = \gamma_{\pm 11}^2 C_{H^+} C_{OH^-} \tag{9}$$

where K_H, K_{hyd}, K_{ca}, K_{bi}, and K_w denote the mathematical description of reaction equilibriums, respectively. The fugacity coefficient (φ) can be determined by the following **Eq. 10**:

$$log\varphi = P\left(0.0031 - \frac{1.4}{T_K}\right) \tag{10}$$

where p was the pressure bar and T_k was the temperature in degrees Kelvin. The temperature-pressure-ionic strength (I) dependence relationship for K_H, K_{hyd}, K_{ca}, K_{bi}, and K_w were listed in **Table 2**, and I was calculated as follows:

$$I = \frac{1}{2}\sum_i m_i z_i^2 \tag{11}$$

where m_i and z_i were the molar concentration and charge of species i, respectively. The mean ionic activity coefficients $\gamma_{\pm 9}$, $\gamma_{\pm 10}$, and $\gamma_{\pm 11}$ in the formation water were 0.662.

In a solution without an externally induced electric field, the concentration of ions must satisfy the electroneutrality constraint. The species Na^{2+}, Ca^{2+}, Mg^{2+}, Cl^-, and SO_4^{2-} dissociated completely in the formation water. Since the addition of $NaHCO_3$ to the formation water would affect the electroneutrality constraint, the charge relationship between ions can be expressed by **Eq. 12**:

$$C_{Na^+} + C_{H^+} = C_{OH^-} + C_{HCO_3^-} + 2C_{CO_3^{2-}} \tag{12}$$

where C_{Na^+} was Na^+ concentration of the artificial addition $NaHCO_3$ in the simulation formation water, and C_{H^+}, C_{OH^-}, $C_{HCO_3^-}$, and $C_{CO_3^{2-}}$ were the equilibrium concentrations of H^+, OH^-, HCO_3^-, and CO_3^{2-}, respectively.

The pH values of FW were calculated as 3.52 and 3.62 at 95°C/2.8 MPa CO_2 and 120°C/3.2 MPa CO_2, respectively.

Surface roughness is of great importance to the chemical and mechanical states at the corrosion interface (Wang et al., 2021). The surface roughness of HP-13Cr SS after FA immersion became larger and increased with the temperature and CO_2 pressure, as is shown in **Figure 11**. At 95°C/2.8 MPa CO_2, the roughness was 3.5 μm (**Figure 11A**), which is quite larger than the roughness of the polishing

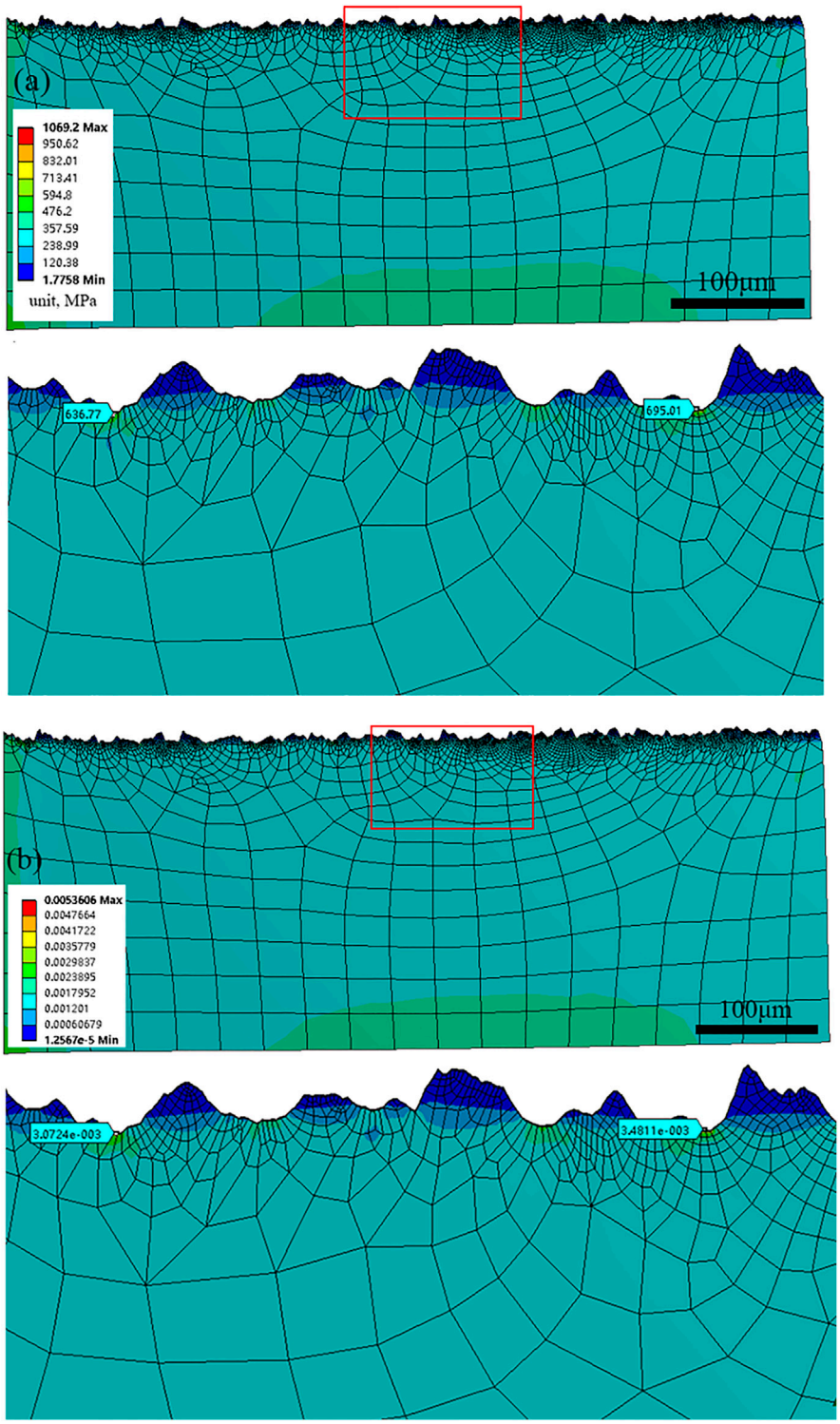

FIGURE 12 | (A) stress and **(B)** strain distribution of the surface after LA immersion at 120°C/3.2 MPa.

surface, without LA immersion, less than 0.1 μm. In addition, the roughness increased to 7.8 μm at 120°C/3.2 MPa (**Figure 11B**). According to the FEM of rough and flat surfaces under 350 MPa tensile stress condition, in **Figure 12**, the stress (**Figure 12A**), and the plastic strain (**Figure 12B**) distribution at 120°C/3.2 MPa were obtained. There was obvious stress and strain concentration in the valley position of the rough surface.

Gutman proposed a kinetic equation for the mechanochemical effect of macroscopic stress on the anodic current i_P of stressed metal (Gutman, 1998),

$$i_P = i_a\left(\frac{\Delta\varepsilon}{\varepsilon_0}+1\right)e^{\frac{PV_m}{RT}} \quad (13)$$

where i_a was the anodic current of stress-free metal, $\Delta\varepsilon$ was the plastic strain, ε_0 was the strain at onset of strain hardening, P was the macroscopic stress, Pa, V_m was molar volume, taken as 7.1×10^{-6} m^3mol^{-1}, R was the gas constant, and T was the temperature, K.

The anodic current in the area with maximum stress and strain concentration was calculated as 1.7 times than that at a flat surface at 120°C/3.2 MPa.

Therefore, the larger roughness caused by LA immersion promoted the local anodic dissolution and then the greater stress and strain concentration occurred. The further increase of stress and strain concentration will further promote the local anodic dissolution, which forms a mutually reinforcing cycle and results in severe SCC (Cui et al., 2016). Moreover, with the temperature/CO_2 pressure increasing from 95°C/2.8 MPa to 120°C/3.2 MPa, the increase in roughness seemed more crucial to SCC than the pH reduction, and eventually, the more severe SCC occurred after higher temperature and CO_2 pressure LA immersion.

CONCLUSION

1. The LA immersion in the acidification process obviously promoted the SCC susceptibility of HP-13Cr SS in FW.
2. With the temperature/CO_2 pressure increasing from 95°C/2.8 MPa to 120°C/3.2 MPa, the surface roughness of HP-13Cr SS after LA immersion increased, resulting in the greater stress concentration and induced the SCC occurring easily.
3. After LA immersion, the interaction of surface roughness, water chemistry, and stress concentration mutually reinforced and deteriorated the SCC of HP-13Cr SS in FW.

DATA AVAILABILITY STATEMENT

The original contributions presented in the study are included in the article/Supplementary Material, further inquiries can be directed to the corresponding author.

AUTHOR CONTRIBUTIONS

WQ: Data curation, Formal analysis, Investigation, Methodology, Validation, Visualization, Writing—original draft. YZ: Investigation, Validation, Visualization, Supervision, Writing—reviewing and editing. TZ: Project administration, Conceptualization, Supervision, Funding, acquisition, Writing—reviewing and editing. FW: Conceptualization, Supervision, Funding acquisition.

ACKNOWLEDGMENTS

The authors express their gratitude to the National Key R&D Research (2017YFB0702203) and National Natural Science Foundation of China (No. 52001061 and No. U1460202) for the long-term support of the programs. The National Program for the Young Top-Notch Professionals and China Postdoctoral Science Foundation (No. 01270012810066) is also acknowledged.

REFERENCES

ASTM (2003). *Standard G1-03, Standard Practice for Preparing Cleaning and Evaluating Corrosion Test Specimens*. West Conshohocken, PA: ASTM International.

Calabrese, L., Bonaccorsi, L., Galeano, M., Proverbio, E., Di Pietro, D., and Cappuccini, F. (2015). Identification of Damage Evolution During SCC on 17-4 PH Stainless Steel by Combining Electrochemical Noise and Acoustic Emission Techniques. *Corrosion Sci.* 98, 573–584. doi:10.1016/j.corsci.2015.05.063

Cui, M., Njoku, D. I., Li, B., Yang, L., Wang, Z., Hou, B., et al. (2021). Corrosion Protection of Aluminium Alloy 2024 Through an Epoxy Coating Embedded With Smart Microcapsules: The Responses of Smart Microcapsules to Corrosive Entities. *Corrosion Commun.* 1, 1–9. doi:10.1016/j.corcom.2021.06.001

Cui, Z. D., Wu, S. L., Li, C. F., Zhu, S. L., and Yang, X. J. (2004). Corrosion Behavior of Oil Tube Steels Under Conditions of Multiphase Flow Saturated With Super-Critical Carbon Dioxide. *Mater. Lett.* 58, 1035–1040. doi:10.1016/j.matlet.2003.08.013

Cui, Z., Liu, Z., Wang, L., Li, X., Du, C., and Wang, X. (2016). Effect of Plastic Deformation on the Electrochemical and Stress Corrosion Cracking Behavior of X70 Steel in Near-Neutral pH Environment. *Mater. Sci. Eng. A.* 677, 259–273. doi:10.1016/j.msea.2016.09.033

Cui, Z. Y., Wang, L. W., Liu, Z. Y., Du, C. W., Li, X. G., and Wang, X. (2011). Anodic Dissolution Behavior of the Crack Tip of X70 Pipeline Steel in Near-Neutral pH Environment. *J. Mater. Eng. Perform.* 20, 1242–1246. doi:10.1007/s11665-016-2394-8

Duan, Z., and Li, D. (2008). Coupled Phase and Aqueous Species Equilibrium of the H2O-CO2-NaCl-CaCO3 System From 0 to 250°C, 1 to 1000bar With NaCl Concentrations up to Saturation of Halite. *Geochimica et Cosmochimica Acta.* 72, 5128–5145. doi:10.1016/j.gca.2008.07.025

Garsany, Y., Pletcher, D., and Hedges, B. (2002). Speciation and Electrochemistry of Brines Containing Acetate Ion and Carbon Dioxide. *J. Electroanalytical Chem.* 538-539, 285–297. doi:10.1016/s0022-0728(02)00728-3

Gutman, E. M. (1998). *Mechanochemistry of Materials*. Cambridge: Cambridge International Science Publishing.

Henthorne, M. (2016). The Slow Strain Rate Stress Corrosion Cracking Test-A 50 Year Retrospective. *Corrosion.* 72, 1488–1518. doi:10.5006/2137

Horner, D. A., Connolly, B. J., Zhou, S., Crocker, L., and Turnbull, A. (2011). Novel Images of the Evolution of Stress Corrosion Cracks from Corrosion Pits. *Corrosion Sci.* 53, 3466–3485. doi:10.1016/j.corsci.2011.05.050

Isaacs, H. S. (1988). Initiation of Stress Corrosion Cracking of Sensitized Type 304 Stainless Steel in Dilute Thiosulfate Solution. *J. Electrochem. Soc.* 135, 2180–2183. doi:10.1149/1.2096235

Lan, X., Lü, X., Zhu, Y., and Yu, H. (2015). The Geometry and Origin of Strike-Slip Faults Cutting the Tazhong Low Rise Megaanticline (Central Uplift, Tarim Basin, China) and Their Control on Hydrocarbon Distribution in Carbonate Reservoirs. *J. Nat. Gas Sci. Eng.* 22, 633–645. doi:10.1016/j.jngse.2014.12.030

Lei, X. W., Feng, Y. R., Fu, A. Q., Zhang, J. X., Bai, Z. Q., Yin, C. X., et al. (2015). Investigation of Stress Corrosion Cracking Behavior of Super 13Cr Tubing by Full-Scale Tubular Goods Corrosion Test System. *Eng. Fail. Anal.* 50, 62–70. doi:10.1016/j.engfailanal.2015.02.001

Li, X. P., Zhao, Y., Qi, W. L., Wang, J. D., Xie, J. F., Wang, H. R., et al. (2019a). Modeling of Pitting Corrosion Damage Based on Electrochemical and Statistical Methods. *J. Electrochem. Soc.* 166, 539–549. doi:10.1149/2.0401915jes

Li, X., Zhao, Y., Qi, W., Xie, J., Wang, J., Liu, B., et al. (2019b). Effect of Extremely Aggressive Environment on the Nature of Corrosion Scales of HP-13Cr Stainless Steel. *Appl. Surf. Sci.* 469, 146–161. doi:10.1016/j.apsusc.2018.10.237

Liu, T., Ma, L., Wang, X., Wang, J., Qian, H., Zhang, D., et al. (2021). Self-Healing Corrosion Protective Coatings Based on Micro/Nanocarriers: A Review. *Corrosion Commun.* 1, 18–25. doi:10.1016/j.corcom.2021.05.004

Lu, Q. K, Wang, L. W., Xin, J. C., Tian, H. Y., Wang, X., and Cui, Z. Y. (2020). Corrosion Evolution and Stress Corrosion Cracking of E690 Steel for Marine Construction in Artificial Seawater Under Potentiostatic Anodic Polarization. *Constr. Build. Mater.* 238, 117763. doi:10.1016/j.conbuildmat.2019.117763

Mai, W., and Soghrati, S. (2017). A Phase Field Model for Simulating the Stress Corrosion Cracking Initiated From Pits. *Corrosion Sci.* 125, 87–98. doi:10.1016/j.corsci.2017.06.006

Marcus, P. (2011). *Corrosion Mechanisms in Theory and Practice*. Boca Raton, FL: CRC Press.

Moreira, R. M., Franco, C. V., Joia, C. J. B. M., Giordana, S., and Mattos, O. R. (2004). The Effects of Temperature and Hydrodynamics on the CO2 Corrosion of 13Cr and 13Cr5Ni2Mo Stainless Steels in the Presence of Free Acetic Acid. *Corrosion Sci.* 46, 2987–3003. doi:10.1016/j.corsci.2004.05.020

Mu, L. J., and Zhao, W. Z. (2010). Investigation on Carbon Dioxide Corrosion Behaviour of HP13Cr110 Stainless Steel in Simulated Stratum Water. *Corrosion Sci.* 52, 82–89. doi:10.1016/j.corsci.2009.08.056

Nordsveen, M., Nešić, S., Nyborg, R., and Stangeland, A. (2003). A Mechanistic Model for Carbon Dioxide Corrosion of Mild Steel in the Presence of Protective Iron Carbonate Films-Part 1: Theory and Verification. *Corrosion.* 59, 443–456. doi:10.5006/1.3277576

Parkins, R. N. (1996). Mechanistic Aspects of Intergranular Stress Corrosion Cracking of Ferritic Steels. *Corrosion.* 52, 363–374. doi:10.5006/1.3292124

Persaud, S. Y., Smith, J. M., and Newman, R. C. (2019). Nanoscale Precursor Sites and Their Importance in the Prediction of Stress Corrosion Cracking Failure. *Corrosion.* 75, 228–239. doi:10.5006/2928

Qi, W. L., Wang, J. D., Li, X. P., Cui, Y. N., Zhao, Y., Xie, J. F., et al. (2021). Effect of Oxide Scale on Corrosion Behavior of HP-13Cr Stainless Steel During Well Completion Process. *J. Mater. Sci. Technology.* 64, 153. doi:10.1016/j.jmst.2019.10.009

Ramamurthy, S., and Atrens, A. (2013). Stress Corrosion Cracking of High-Strength Steels. *Corros. Rew.* 31, 1–31. doi:10.1515/corrrev-2012-0018

Singh, A., Ansari, K. R., Kumar, A., Liu, W., Songsong, C., and Lin, Y. (2017). Electrochemical, Surface and Quantum Chemical Studies of Novel Imidazole Derivatives as Corrosion Inhibitors for J55 Steel in Sweet Corrosive Environment. *J. Alloys Compounds.* 712, 121–133. doi:10.1016/j.jallcom.2017.04.072

Song, G.-L., Zhang, C., Chen, X., and Zheng, D. (2021). Galvanic Activity of Carbon Fiber Reinforced Polymers and Electrochemical Behavior of Carbon Fiber. *Corrosion Commun.* 1, 26–39. doi:10.1016/j.corcom.2021.05.003

Spencer, D. T., Edwards, M. R., Wenman, M. R., Tsitsios, C., Scatigno, G. G., and Chard-Tuckey, P. R. (2014). The Initiation and Propagation of Chloride-Induced Transgranular Stress-Corrosion Cracking (TGSCC) of 304L Austenitic Stainless Steel Under Atmospheric Conditions. *Corrosion Sci.* 88, 76–88. doi:10.1016/j.corsci.2014.07.017

Suter, T., Webb, E. G., Bo̎hni, H., and Alkire, R. C. (2001). Pit Initiation on Stainless Steels in 1 M NaCl With and Without Mechanical Stress. *J. Electrochem. Soc.* 148, B174–B185. doi:10.1149/1.1360204

Tian, H., Wang, X., Cui, Z., Lu, Q., Wang, L., Lei, L., et al. (2018). Electrochemical Corrosion, Hydrogen Permeation and Stress Corrosion Cracking Behavior of E690 Steel in Thiosulfate-Containing Artificial Seawater. *Corrosion Sci.* 144, 145–162. doi:10.1016/j.corsci.2018.08.048

Wang, H., and Han, E.-H. (2013). Simulation of Metastable Corrosion Pit Development Under Mechanical Stress. *Electrochimica Acta.* 90, 128–134. doi:10.1016/j.electacta.2012.11.056

Wang, L., Xin, J., Cheng, L., Zhao, K., Sun, B., Li, J., et al. (2019). Influence of Inclusions on Initiation of Pitting Corrosion and Stress Corrosion Cracking of X70 Steel in Near-Neutral pH Environment. *Corrosion Sci.* 147, 108–127. doi:10.1016/j.corsci.2018.11.007

Wang, P., Chen, X., Li, T., Cai, H., and Zhang, D. (2021). Exceptional Atmospheric Corrosion Inhibition Performance of Super-Hydrophobic Films Based on the Self-Propelled Jumping Behavior of Water Droplets. *Corrosion Commun.* 1, 40–46. doi:10.1016/j.corcom.2021.06.002

Yue, X., Zhao, M., Zhang, L., Zhang, H., Li, D., and Lu, M. (2018). Correlation Between Electrochemical Properties and Stress Corrosion Cracking of Super 13Cr under an HTHP CO2 Environment. *RSC Adv.* 8, 24679–24689. doi:10.1039/c8ra04222e

Zhang, G. A., and Cheng, Y. F. (2009). On the Fundamentals of Electrochemical Corrosion of X65 Steel in CO2-Containing Formation Water in the Presence of Acetic Acid in Petroleum Production. *Corrosion Sci.* 51, 87–94. doi:10.1016/j.corsci.2008.10.013

Zhang, S., Li, H., Jiang, Z., Zhang, B., Li, Z., Wu, J., et al. (2020). Chloride- and Sulphate-Induced Hot Corrosion Mechanism of Super Austenitic Stainless Steel S31254 Under Dry Gas Environment. *Corrosion Sci.* 163, 108295. doi:10.1016/j.corsci.2019.108295

Zhang, Z., Zheng, Y., Li, J., Liu, W., Liu, M., Gao, W., et al. (2019). Stress Corrosion Crack Evaluation of Super 13Cr Tubing in High-Temperature and High-Pressure Gas wells. *Eng. Fail. Anal.* 95, 263–272. doi:10.1016/j.engfailanal.2018.09.030

Zhao, W. M., Xin, R. F., He, Z. R., and Wang, Y. (2012). Contribution of Anodic Dissolution to the Corrosion Fatigue Crack Propagation of X80 Steel in 3.5 wt.% NaCl Solution. *Corros. Sci.* 63, 387–392. doi:10.1016/j.corsci.2012.06.016

Zhao, Y., Xie, J., Zeng, G., Zhang, T., Xu, D., and Wang, F. (2019a). Pourbaix Diagram for HP-13Cr Stainless Steel in the Aggressive Oilfield Environment Characterized by High Temperature, High CO2 Partial Pressure and High Salinityfield Environment Characterized by High Temperature, High CO_2 Partial Pressure and High Salinity. *Electrochimica Acta.* 293, 116–127. doi:10.1016/j.electacta.2018.08.156

Zhao, Y., Cao, S.-Y., Zhang, T., Xie, J.-F., Xu, D.-K., and Wang, F.-H. (2019b). A New High-Efficiency Experimental Design for Optimizing Various Flow Velocities Testing in Extremely Aggressive Formation Water. *Acta Metall. Sin. Engl. Lett.* 32, 944–950. doi:10.1007/s40195-019-00919-x

Zhao, Y., Li, X., Zhang, C., Zhang, T., Xie, J., Zeng, G., et al. (2018). Investigation of the Rotation Speed on Corrosion Behavior of HP-13Cr Stainless Steel in the Extremely Aggressive Oilfield Environment by Using the Rotating Cage Test. *Corrosion Sci.* 145, 307–319. doi:10.1016/j.corsci.2018.10.011

Zhao, Y., Qi, W., Xie, J., Chen, Y., Zhang, T., Xu, D., et al. (2020). Investigation of the Failure Mechanism of the TG-201 Inhibitor: Promoting the Synergistic Effect of HP-13Cr Stainless Steel During the Well Completion. *Corrosion Sci.* 166, 108448. doi:10.1016/j.corsci.2020.108448

Zhu, S. D., Wei, J. F., Cai, R., Bai, Z. Q., and Zhou, G. S. (2011). Corrosion Failure Analysis of High Strength Grade Super 13Cr-110 Tubing String. *Eng. Fail. Anal.* 18, 2222–2231. doi:10.1016/j.engfailanal.2011.07.017

Conflict of Interest: The authors declare that the research was conducted in the absence of any commercial or financial relationships that could be construed as a potential conflict of interest.

Publisher's Note: All claims expressed in this article are solely those of the authors and do not necessarily represent those of their affiliated organizations, or those of the publisher, the editors and the reviewers. Any product that may be evaluated in this article, or claim that may be made by its manufacturer, is not guaranteed or endorsed by the publisher.